batteries

MDPI

Article

In Situ Formation of Li-Ag Alloy Thin Film for Stabilized Ultra-Thin Lithium Metal Anodes

Hyunyoung Kim [1], Saac Lee [2], Chi Won Ahn [2], Hee Han [2], Youngwoo Choi [3], Seungbum Hong [3], Sung-Soo Kim [1,*], Hyeyoung Shin [1,4,*] and Su-Ho Cho [2,*]

[1] Graduate School of Energy Science and Technology, Chungnam National University, 99 Daehak-ro, Yuseong-gu, Daejeon 34134, Republic of Korea; gusddud18@naver.com
[2] National Nanofab Center, 291 Daehak-ro, Yuseong-gu, Daejeon 34141, Republic of Korea; leeisaac803@nnfc.re.kr (S.L.); cwahn@nnfc.re.kr (C.W.A.); hhan@nnfc.re.kr (H.H.)
[3] Department of Materials Science and Engineering, Korea Advanced Institute of Science and Technology (KAIST), 291 Daehak-ro, Yuseong-gu, Daejeon 34141, Republic of Korea; slpdavid@kaist.ac.kr (Y.C.); seungbum@kaist.ac.kr (S.H.)
[4] Department of Chemistry, College of Sciences, Kyung Hee University, 26 Kyungheedae-ro, Dongdaemun-gu, Seoul 02447, Republic of Korea
* Correspondence: kimss@cnu.ac.kr (S.-S.K.); shinhy@khu.ac.kr (H.S.); csh0160@nnfc.re.kr (S.-H.C.)

Abstract

Lithium (Li) metal anodes are fundamental to the development of next-generation high-energy-density batteries, yet their practical use is severely limited by uncontrolled dendrite growth and interfacial instability. This study proposes an effective strategy to stabilize the Li metal interface through the in situ formation of a Li-Ag alloy using a sequential thermal evaporation process. By depositing an Ag seed layer as a lithiophilic template prior to Li evaporation, the nucleation barrier is significantly reduced, facilitating more uniform and dense lithium deposition. The morphological evolution and pristine surface chemical states of the evaporated layers were investigated under air-free conditions to confirm the compositional integrity of the alloyed interface. Electrochemical evaluations in symmetric cells demonstrate that the Li-Ag alloy phase effectively regulates Li-ion flux, reducing the surface roughness by approximately 30% and leading to a markedly lower overpotential and more than a two-fold extension of cycle life compared to pure evaporated Li. These results indicate that precision-controlled vacuum deposition and in situ alloying are viable approaches for engineering high-performance interfaces, providing a robust foundation for more reliable and dendrite-suppressed lithium metal battery systems.

Keywords: Li-ion batteries; Li metal anodes; thin film electrode; Li-Ag alloy

Check for updates

Academic Editor: Maziar Ashuri

Received: 9 October 2026
Revised: 1 November 2026
Accepted: 3 November 2026
Published: 17 November 2026

Copyright: © 2026 by the authors. Licensee MDPI, Basel, Switzerland. This article is an open access article distributed under the terms and conditions of the Creative Commons Attribution (CC BY) license.

1. Introduction

Rapid industrial advancement has significantly increased the demand for energy storage systems with both high energy density and high power capability [1,2]. Consequently, various applications, including electric vehicles, portable electronics, and large-scale energy storage systems, require batteries with enhanced energy density. However, the conventional graphite anode used in lithium-ion batteries is approaching its theoretical capacity limit, highlighting the necessity for the development of alternative anode materials [3–5].

Among the promising candidates, lithium (Li) metal has attracted considerable attention. Li metal batteries have emerged as next-generation energy storage systems due to the exceptional properties of Li metal, including its high theoretical capacity (3860 mAh g^{-1}) and the lowest electrochemical potential (−3.04 V vs. SHE) [6–8]. Despite these

advantages, the practical application of Li metal anodes is hindered by severe volume changes during cycling and the formation of lithium dendrites, which lead to poor cycling stability and safety concerns [6,9,10]. To address these challenges, various strategies have been extensively investigated, such as inducing uniform lithium deposition and stabilizing the solid-electrolyte-interphase (SEI) through lithiophilic alloy layers [11], electrolyte additives [12], and three-dimensional host structures [13].

In addition, Li metal is typically used in excess in practical systems, which reduces the overall energy density due to increased cell weight [14–16]. Conventionally, Li metal anodes are fabricated by rolling bulk Li metal into thin foils. However, the rolling process has inherent limitations in reducing foil thickness below approximately 20 μm because of the poor mechanical properties of Li metal [15]. Furthermore, exposure to the manufacturing environment can introduce surface impurities and native passivation layers, resulting in reduced material purity and inferior electrochemical performance [14,17].

Previous studies have introduced Ag through solution-based routes. Hou et al. formed lithiophilic Ag nanoparticles on Cu foil by electroless plating, which reduced the Li nucleation overpotential from 240 to 52 mV, and 10 mAh cm^{-2} of Li was subsequently supplied by electrodeposition [18]. Park et al. coated a 2–3 μm thick Ag nanoparticle/PVdF-HFP layer on Cu and electrodeposited 4.0 mAh cm^{-2}, or 20 μm, of Li to form a Li-Ag alloy with an in situ formed SEI for all-solid-state batteries [19]. In both cases, Ag is introduced by wet processing, the alloy is formed electrochemically, and the Li inventory corresponds to 20–50 μm. In contrast, the present work forms the Li-Ag alloy entirely by dry, sequential vacuum deposition without solvents, binders, or electrochemical pre-plating, and evaluates the effect of Ag on ultra-thin Li films of only 5–10 μm, corresponding to about 1–2 mAh cm^{-2}. Furthermore, we quantify the Li consumed by alloying, which defines the trade-off between interfacial stabilization and acive Li loss in the ultra-thin regime.

In this study, Li metal thin films were fabricated via thermal evaporation, a physical vapor deposition method in which Li metal is vaporized by resistive heating under high vacuum and subsequently deposited onto a substrate [20]. This technique offers several advantages, including high purity enabled by the difference in boiling points between lithium and impurities, precise thickness control from nanometer to micrometer scale, and contamination-free processing within an inert glove box environment [17,20]. Nevertheless, Li films prepared by thermal evaporation often exhibit rough surface morphology and poor uniformity, which can degrade ionic conductivity and promote dendrite formation, particularly in solid-state battery systems [21,22].

To overcome these limitations, we propose the formation of a Li–Ag alloy structure at the interface via a sequential layer-by-layer deposition process using thermal evaporation. In this approach, Ag and Li are deposited alternately, which enhances the adhesion between the Li metal and the current collector while simultaneously improving structural uniformity. Ag, a lithiophilic metal, readily forms alloys with lithium and possesses high electrical conductivity and strong affinity for lithium, enabling effective regulation of lithium nucleation and growth behavior [11,18]. In addition, the introduction of a silver interlayer promotes uniform lithium deposition and enhances interfacial stability, thereby suppressing dendrite formation [18,19]. Consequently, this layer-by-layer alloy structure can serve as an effective strategy to improve the cycling stability of lithium metal anodes.

2. Materials and Methods

2.1. Anode Deposition via Thermal Evaporation

All deposition processes were carried out using the specialized battery deposition system (SRN-100, Sorona, South Korea) at the National NanoFab Center (NNFC) in South Korea. Copper (Cu) foil substrates were cleaned and used as current collectors for Li

metal thin films. For the thermal evaporation deposition of lithium metal, high-purity lithium granules (NEBA, 99.9%) were placed in a molybdenum (Mo) boat and loaded into a vacuum chamber, which was evacuated to a base pressure of approximately 10^{-7} Torr prior to thermal evaporation. Thermal evaporation was then carried out by gradually increasing the temperature of Mo boat until lithium evaporation was initiated. When the deposition rate reached 10.0 Å s^{-1}, the shutter was opened and the lithium metal film was deposited at a constant rate of 10.0 Å s^{-1} to a target thickness of 5 μm and 10 μm, as monitored by a quartz crystal microbalance (QCM).

For the fabrication of the Ag underlayer, Cu foil substrates were similarly prepared. The Ag layers were first deposited onto the Cu foil at a rate of 2.0 Å s^{-1} to a thickness of 1.0 μm and 2.0 μm, as measured by QCM, respectively. A Li layer was deposited on top of the Ag layer under the same conditions described above, yielding Li-Ag layer-by-layer structure without breaking vacuum.

2.2. Electrochemical Measurements

Electrochemical performance was evaluated using CR2032-type coin cells assembled in an argon-filled glove box with oxygen and moisture levels below 0.1 ppm. A polypropylene separator (Celgard 2400, Celgard, LLC, Japan) was used, and the electrolyte consisted of 1 M $LiPF_6$ in ethylene carbonate and diethyl carbonate (EC/DEC, v/v = 1:1) with 5 wt% fluoroethylene carbonate (FEC) additive.

For symmetric cell tests, deposited Li and Li–Ag electrodes were assembled in a symmetric configuration (Li//Li and Li–Ag//Li–Ag). Galvanostatic cycling was performed at current densities of 0.1 and 0.5 mA cm^{-2} with a fixed plating/stripping duration of 1 h per half-cycle. The cells were cycled for up to 200 cycles to evaluate interfacial stability and dendrite suppression behavior.

To electrochemically verify alloy formation, the as-deposited Li and Li-Ag films were galvanostatically delithiated at 0.05 mA cm^{-2} to a cut-off voltage of 1.0 V vs. Li/Li^+ in half cells with a Li foil counter electrode. As a reference, an Ag-only electrode (Ag 1 μm evaporated on Cu foil) was lithiated at 0.05 mA cm^{-2} to 0.01 V, held potentiostatically at 0.01 V to complete alloying, and then delithiated to 1.0 V. dQ/dV curves were obtained from the voltage profiles.

For full-cell measurements, Li–Ag electrodes were paired with a $LiNi_{0.8}Co_{0.1}Mn_{0.1}O_2$ (NCM811) cathode with an areal capacity of 1.0 mAh cm^{-2}. The cells were cycled at 0.5 C within a voltage window of 2.9~4.2 V to assess electrochemical performance. All electrochemical measurements were conducted using a battery testing system (WonATech, WBCS3000, South Korea).

Electrochemical impedance spectroscopy (EIS) was performed on symmetric cells before cycling and after 10 and 50 cycles over a frequency range of 1 MHz to 100 mHz with an AC amplitude of 10 mV. The distribution of relaxation time (DRT) was calculated using Tikhonov regularization and the spectra was fitted with the equivalent circuit derived from the DRT analysis.

2.3. Morphological and Compositional Characterization

The morphology of the deposited Li and Li–Ag electrodes was analyzed using scanning electron microscopy (SEM). Cross-sectional and surface images were obtained to investigate the structural features and uniformity of the deposited layers. Elemental distribution was examined by energy-dispersive X-ray spectroscopy (EDS) mapping.

To prevent degradation of lithium metal, all samples were transferred and analyzed under air-free conditions without exposure to ambient atmosphere. The samples were handled using an inert transfer system (e.g., vacuum transfer vessel or glove box transfer

module) to minimize contamination and oxidation. For XPS analysis, the samples were mounted on an air-tight transfer holder inside the glove box and transferred to the spectrometer without exposure to ambient air (Figure S3a). XPS depth profiling was performed by Ar^+ ion sputtering, and high-resolution Li 1s, Ag 3d, Ag MNN, O1s, C 1s, and Cu 2p spectra were acquired at each sputtering step. The modified Auger parameter of Ag was calculated as the sum of the Ag $3d_{5/2}$ binding energy and Ag MNN kinetic energy. An Ag-only film and a pristine Li film were measured under identical conditions as references, and binding energies were calibrated to the C 1s peak at 284.8 eV.

Surface morphology and roughness were further characterized by atomic force microscopy (AFM), also conducted under air-free or inert conditions to preserve the intrinsic surface properties of lithium.

3. Results and Discussions

3.1. Design and Fabrication of the Li-Ag Layer-by-Layer Electrode

Figure 1 represents the overall design concept and fabrication strategy of the Li-Ag layer-by-layer electrode. As shown in Figure 1a, a dual-source thermal evaporation chamber was employed, in which a Li metal source (Source 1) and an Ag source (Source 2) were independently loaded into separate Mo boats beneath a common Cu foil substrate. The chamber was evacuated to a base pressure of ~10^{-7} Torr to minimize residual oxygen and moisture, and the deposition rate and thickness of each metal were monitored in real time by a QCM. This configuration enables sequential deposition of the two metals without breaking vacuum, ensuring that freshly formed Ag surface remains free of native oxide prior to Li evaporation.

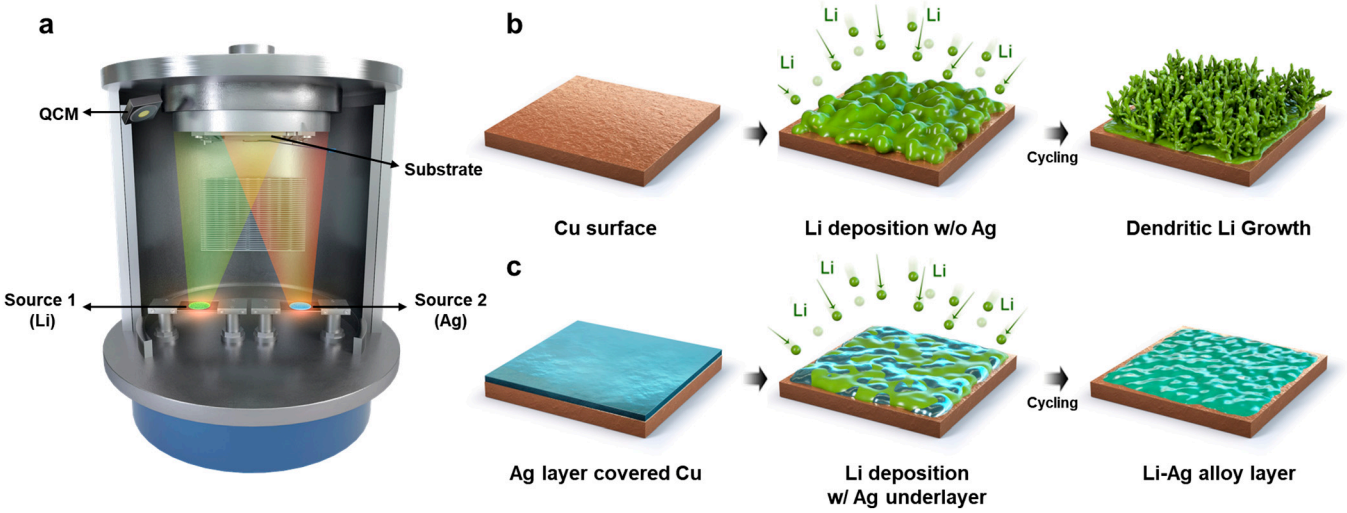


Figure 1. (**a**) Schematic illustration of the dual-source thermal evaporation system used for the sequential deposition of Li and Ag, (**b**) deposition of Li directly on bare Cu, which leads to dendritic Li growth after cycling, (**c**) deposition of Li on an Ag-coated Cu, which forms a Li-Ag alloy layer that remains dense and dendrite-free after cycling.

The role of the pre-deposited Ag interlayer is schematically compared in Figure 1b,c. In the absence of an Ag seed layer (Figure 1b), Li vapor impinges directly on the bare Cu surface, which has poor lithiophilicity and a large heterogeneous nucleation barrier. The resulting deposited film is compositionally pure Li but morphologically non-uniform; upon subsequent plating/stripping, the low-affinity Li/Cu interface promotes localized current crowding and dendritic/mossy Li growth, ultimately leading to internal short-circuiting. In contrast, when a thin Ag underlayer is first deposited on the Cu current collector (Figure 1c),

incoming Li atoms encounter a lithiophilic template and are immediately alloyed in situ to form a Li-Ag solid solution. Because the Li-Ag binary system exhibits an exceptionally low nucleation overpotential and a high solubility of Li in Ag, the deposited film grows as a dense, conformal film rather than as isolated islands. During subsequent cycling, this Li-Ag alloy layer functions as a buffer that homogenizes Li-ion flux, suppresses dendrite initiation, and preserves intimate electrical contact with the Cu current collector.

The thermodynamic basis for this room temperature alloying can be understood from the Li-Ag binary phase diagram [23]. The Li-Ag system contains an Ag-rich fcc solid solution, the β-LiAg phase, a series of Li-rich γ phases, and a Li-rich bcc solid solution, all of which are stable at room temperature and possess wide homogeneity ranges. Owing to the negative enthalpy of mixing and the high diffusivity of Li, Li atoms arriving on the Ag surface can react and interdiffuse without external heating, progressively converting Ag into Li-richer phases as the Li supply increases. Unlike Li-Zn or Li-Al, the Li-Ag system accommodates composition changes through broad solid solution ranges with minimal structural change [23], which is consistent with the continuous, conformal morphology observed here. The alloy formation is examined spectroscopically and electrochemically with XPS and electrochemical dealloying tests.

3.2. Morphological and Compositional Characterization

The morphology of the deposited Li and Li–Ag electrodes was analyzed using scanning electron microscopy (SEM) and atomic force microscopy (AFM) (Figure 2a–f). Cross-sectional SEM images (Figure 2a) show that the Li-only film deposited on bare Cu presents a loosely packed, porous structure with a poorly defined interface between the current collector and the deposited film. In contrast, the Li-Ag film exhibits strong adhesion to the Cu substrate, attributable to the Ag underlayer and the resulting alloy formation. (Figure 2d,e) However, when the deposition sequence is reversed and the Ag layer is deposited on top of the Li film, the surface exhibits markedly higher non-uniformity, with irregular network-like features and pronounced Li grain growth (Figure S2). This comparison indicates that the deposition sequence is critical. The Ag underlayer serves as a lithiophilic surface that guides uniform Li growth from the current collector side, whereas an Ag overlayer cannot regulate the growth of the underlying Li film and instead aggravates surface heterogeneity.

The quantitative impact of the Ag underlayer on surface topography is confirmed by AFM (Figure 2c,f). The arithmetic mean roughness of the evaporated Li film is Ra = 347.81 nm, whereas that of the Li-Ag film is decreased to Ra = 244.17 nm, corresponding to an approximately 30% reduction. This smoother topography directly translates into a more homogeneous local current density during plating/stripping, mitigating the hot-spot driven nucleation of Li dendrites. The lower Ra of the Li-Ag film is fully consistent with the SEM observations and supports the phenomenon that in situ alloy formation provides a thermodynamically favorable template for uniform Li deposition during thermal evaporation process.

Cross-sectional EDS elemental mapping (Figure 2g) of the Li-Ag electrode reveals the spatial distribution of Ag across the layered stack. The distribution of Cu is confined to the bottom of the cross section for current collector, while the Ag atoms appear as a continuous, sharply defined band immediately above the Cu, confirming that the pre-deposited Ag layer remains laterally continuous after the subsequent Li evaporation. Importantly, no significant Cu/Ag interdiffusion is detected, verifying that the layer-by-layer architecture (C/Li-Ag alloy) is preserved after deposition and that the alloying reaction is confined to the Li-Ag interface as intended. Due to the low sensitivity of Li in EDS analysis, direct mapping of Li is not feasible; however, the total thickness of the Li-Ag layer is estimated to be approximately 6 μm. Although the Ag layer was initially deposited with a thickness of

~1 µm at the bottom region, it is observed to be distributed throughout the entire layer. This indicates that the Li-Ag alloying reaction occurred throughout the thickness of the electrode. This spontaneous alloying is also evident from the change in the electrode appearance during storage (Figure S1). Immediately after deposition, both the Li and Li-Ag films (1 µm Li with or without a 100 nm Ag layer) exhibited a metallic luster. After storage for 24 h under an Ar atmosphere, however, the Ag-containing film turned uniformly dark, whereas the Ag-free Li film retained its silvery appearance. Because the samples were kept under an inert atmosphere, this color change is unlikely to originate from oxidation and is instead attributed to solid-state interdiffusion and alloying between Li and Ag at room temperature.

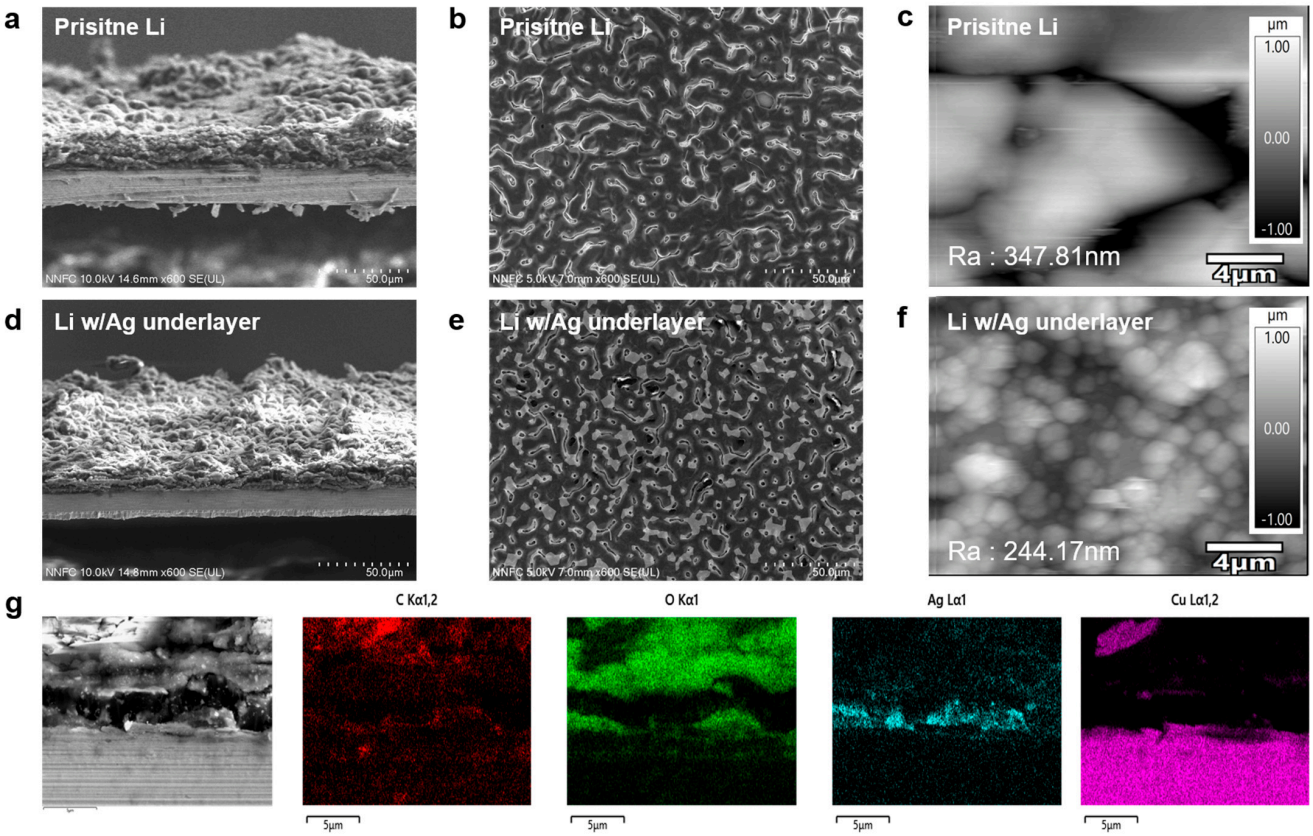


Figure 2. Morphological and compositional characterization of the evaporated electrodes. Cross-sectional and topview SEM images of the Li (**a**,**b**) and Li/Ag (**d**,**e**) films. AFM topography of the corresponding surfaces, showing a decrease in arithmetic roughness from (**c**) Ra = 347.81 nm (Li) to (**f**) 244.17 nm (Li/Ag). (**g**) Cross-sectional SEM image of the Li/Ag electrode and the corresponding EDS elemental mapping of C, O, Ag, and Cu.

3.3. Surface Chemistry of Li-Ag Alloy Formation

To confirm the chemical state of the deposited films and verify the in situ formation of the Li-Ag alloy by continuous evaporation processes, air-free X-ray photoelectron spectroscopy (XPS) was performed on both Li and Li-Ag electrodes (Figures 3 and S3). The survey spectra of both electrodes (Figure S3b) are dominated by Li 1s, C 1s, and O 1s, the latter two arising from the native surface layer that forms even under inert conditions. The Ag3d signal is not resolved in the survey scan and is detected only in the high-resolution spectrum, indicating a relatively low Ag concentration within the probed surface region. In the Ag 3d region, the Li-Ag electrode (Figure 3a) exhibits clearly resolved doublet peaks with Ag 3d5/2 and Ag 3d3/2 peaks at approximately 368.1 and 374.1 eV, respectively.

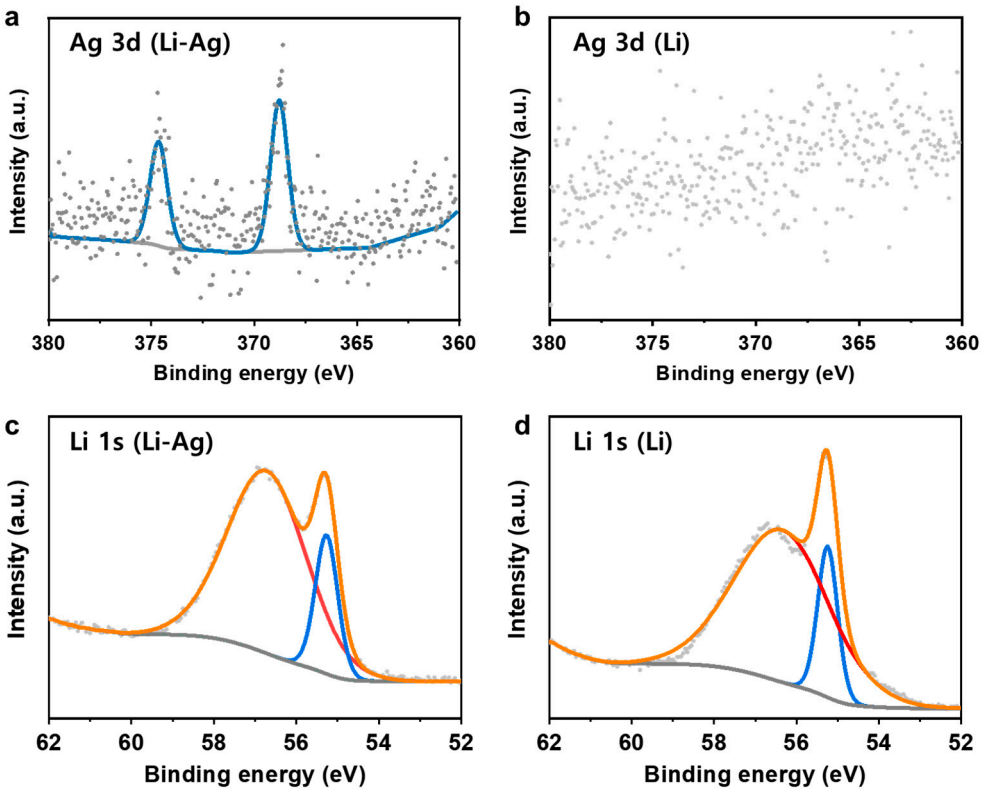


Figure 3. XPS spectra of the evaporated electrodes. (**a**) Ag 3d and (**c**) Li 1s spectra of the Li/Ag electrode, (**b**) Ag 3d and (**d**) Li 1s spectra of pristine Li electrode. (Ag 3d—Gray dots: raw data, gray line: background, blue curves: Ag 3d peaks; Li 1s—Orange curve: fitted lines, blue line: Li metallic peak, red line: Li^+ peaks).

These binding energies are slightly shifted relative to those of pure metallic Ag, consistent with charge redistribution upon Li-Ag alloying. However, because the Ag 3d shift accompanying Li-Ag alloying is small and close to the binding energy of metallic Ag at 368.2–368.3 eV, the Ag 3d position alone cannot unambiguously distinguish an alloy from metallic Ag. For comparison, a shift in Ag 3d5/2 to 367.4 eV has been reported for an electrodeposited Li-Ag alloy [19]. We therefore additionally analyzed the Ag MNN Auger transition and depth profiles. By contrast, the pristine Li electrode (Figure 3b) shows only baseline noise in the same region, confirming the absence of Ag in the pristine Li sample and verifying that the Ag peak in the Li-Ag electrode originates from the alloyed structure rather than from surface contamination.

Notably, despite the surface-sensitive analytical nature of XPS, distinct Ag peaks are still observed from the Li-Ag electrode. This suggests that Ag is not confined to the initially deposited bottom layer but is redistributed toward the surface region as a result of alloying with Li. Such upward redistribution of Ag, accompanied by the observed binding energy shift, supports for the formation of a Li-Ag alloy during the Li deposition process.

The Li 1s spectra also provides the characteristic of alloying reaction between Li and Ag. The Li 1s spectra of the Li-Ag electrode (Figure 3c) can be deconvoluted into two main components including a sharp peak at 55.2 eV that is assignable to metallic Li, and a broader peak near 56–57 eV that is attributable to Li in an electron-deficient chemical environment. The electron density is partially transferred from Li to the more electronegative Ag, when they form the alloying structure. The pristine Li electrode (Figure 3d) shows a comparatively narrower metallic Li 1s peak and the broaden peak dominated usual surface species (Li_2O, Li_2CO_3, etc.). Collectively, the XPS results corroborate that a Li-Ag alloy phase forms in situ at the buried interface, rather than a simple Li-on-Ag bilayer.

To distinguish alloying from simple Li/Ag interfacial mixing, air-free XPS depth profiles of the Li-Ag/Cu electrode were compared with those of the Li/Cu and Ag/Cu reference electrodes, and the modified Auger parameter of Ag reference electrode (α' = Binding energy of Ag $3d_{5/2}$ + Kinetic energy of Ag $M_4N_{45}N_{45}$) was evaluated (Figure S4). In the Li-Ag/Cu electrode, the Ag appears from an early stage of sputtering and increases gradually without any pure Ag region, indicating that Ag is distributed within the Li layer rather than remaining as a discrete interlayer. Because the Li containing surface species of this electrode showed differential charging (~3 eV), the chemical state of Ag was evaluated using the charge independent α'. Auger parameter increases from 726.1 eV for the metallic Ag/Cu electrode to 727.0 eV for Li-Ag/Cu, a shift opposite to that of Ag oxides (~724.5 eV) [24], indicating that Ag remains metallic but in a chemical environment different from pure Ag, consistent with Li-Ag alloying. The higher bulk Li/O ratio of Li-Ag/Cu (2.41 vs. 1.83 for Li/Cu_) further indicates a larger fraction of metallic Li.

Electrochemical dealloying test was conducted for alloy phase analysis (Figure S5). After the stripping of metallic Li, the Li-Ag electrode shows a distinct plateau at ~0.30 V, which matches the dealloying plateau of the electrochemically lithiated Ag electrode and is absent for the pristine Li electrode, confirming that a Li-Ag alloy was already present in the as-deposited film. The dealloying capacity (0.08–0.14 mAh cm^{-2}, Li_xAg with $x \approx 0.32$–0.54) corresponds to 55–92% of that of the lithiated Ag electrode ($x \approx 0.59$), indicating that most of the Ag layer was alloyed during deposition. These spectroscopic and electrochemical results together support the in situ formation of a Li-Ag alloy rather than a simple Li on Ag bilayer.

3.4. Electrochemical Performance in Symmetric Cells

The electrochemical stability of the Li-Ag alloy electrode was evaluated in symmetric Li//Li and Li-Ag//Li-Ag cells with liquid electrolyte (Figure 4). In Figure 4a–d, at a moderate current density of 0.1 mA cm^{-2} with a plating/stripping duration of 1 h per half cycle (0.1 mAh cm^{-2}), the pristine Li electrode initially cycles with a narrow polarization of 10 mV but develops large, erratic voltage fluctuations after 100 cycles and experiences a soft short-circuit after 120 cycles, characteristic of catastrophic dendritic failure. In contrast, the Li-Ag electrode maintains stable and symmetric voltage curves with an overpotential of about 15 mV throughout 200 cycles without any sign of failure, indicating a substantially longer cycling life than the pristine Li electrode.

Magnified graphs of initial 10 cycles (Figure 4b) and between 50th cycle and 60th cycle (Figure 4c) reveal that the two electrodes represent comparable polarization in the initial few cycles, but the Li-Ag electrode reaches steady-state behavior with flat, well-defined voltage plateaus rapidly. The slightly higher polarization of the Li-Ag electrode in the first cycles, shown in Figure 4b, is attributed to the concurrent further alloying of Ag with Li and the initial SEI formation on the alloy surface. Once these processes are complete, the Li-Ag electrode exhibits lower and more stable polarization than the pristine Li electrode. This is consistent with the role of the lithiophilic Ag underlayer in lowering the Li nucleation barrier and providing a continuous, ion permeable interface from the first cycle. In the late stage (cycles between 120th and 130th cycle, Figure 4d), the pristine Li electrode shows markedly increased and asymmetric polarization with sharp voltage spikes at the onset of every cycle, characteristic of a porous, dendritic Li morphology that continuously consumes electrolyte and Li through repeated SEI fracture and formation. The Li-Ag electrode, by comparison, retains smooth, square-shaped voltage profiles, indicating that the Li-Ag alloy interface preserves a chemically and mechanically stable SEI formation.

Under the more aggressive condition of 0.5 mA cm^{-2} (Figure 4e), the advantage of the Li-Ag alloy interface becomes even more pronounced. The pristine Li electrode short-circuits

at 22 cycles, whereas the Li-Ag electrode sustains stable cycling up to 55 cycles. The initial 10 cycles (Figure 4f) show that the Li-Ag electrode consistently exhibits a lower nucleation overpotential than the Li-only cell. The results of the symmetric cell tests demonstrate that the in situ Li–Ag alloy strategy robustly regulates Li-ion flux and suppresses dendrite growth under tested conditions.

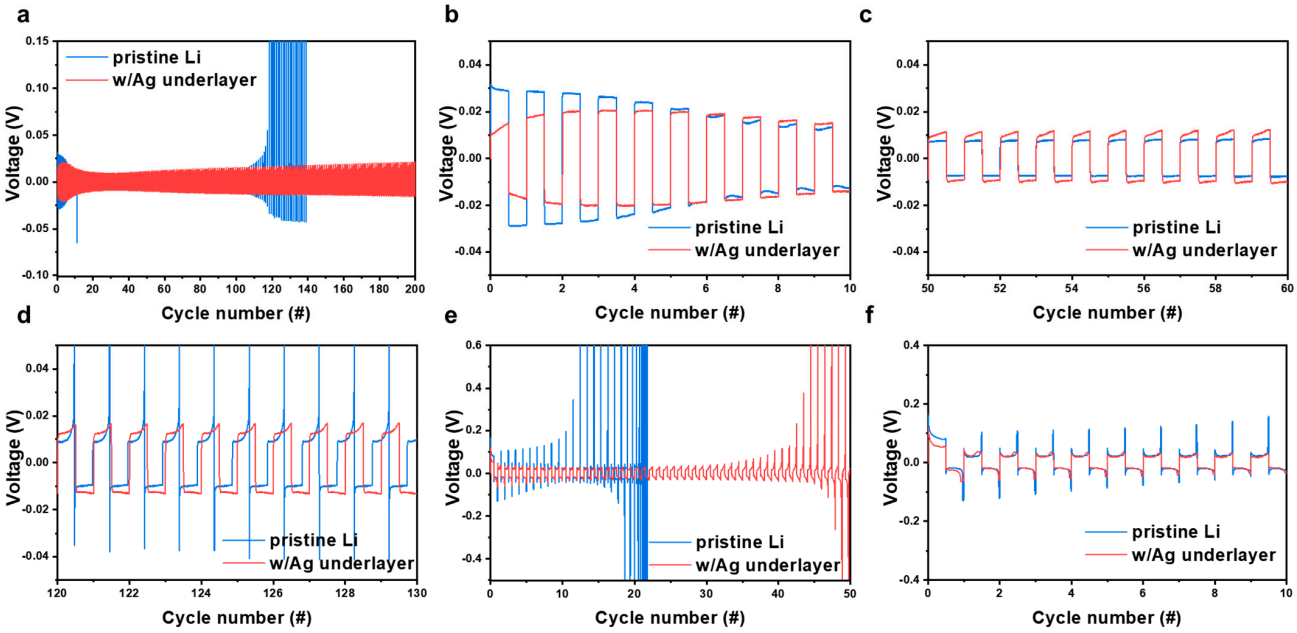


Figure 4. Galvanostatic cycling of symmetric cells. (**a**) Long-term plating/stripping test at 0.1 mA cm^{-2} with 0.1 mAh cm^{-2}. (**b**–**d**) Magnified profiles of the initial, middle, and late stages of (**a**). (**e**) Long-term plating/stripping test at 0.5 mA cm^{-2} with 0.5 mAh cm^{-2}. (**f**) Magnified profiles of the initial cycles of (**e**).

Because symmetric cells do not directly measure the nucleation barrier, the symmetric cell results are discussed in terms of overpotential, and the reduction in the Li nucleation overpotential on lithiophilic Ag surfaces, for example from 240 to 52 mV on Ag-decorated Cu, has been directly demonstrated in previous studies [18]. We note that the current densities of 0.1–0.5 mA cm^{-2} and areal capacities of 0.1–0.5 mAh cm^{-2} used here were chosen considering the limited Li inventory of the ultra-thin films, about 1.03 mAh cm^{-2} for 5 μm Li.

3.5. EIS Analysis and FIB-SEM in Symmetric Cells

To further probe the interfacial origin of the electrochemical differences observed above, electrochemical impedance spectroscopy (EIS) and cross-sectional FIB-SEM imaging were performed on the symmetric cells before cycling, after 10 cycles, and after 50 cycles (Figure 5). Before cycling (Figure 5a), the Nyquist plot of the pristine Li cell shows a broad response that closes at a real-axis value of approximately 750 Ω, whereas the Li-Ag cell exhibits a substantially smaller response, closing at approximately 450 Ω. This roughly 40% reduction in total interfacial impedance, present even prior to any electrochemical cycling, indicates that the in situ alloyed interface intrinsically provides a lower-resistance pathway for Li-ion transport, consistent with the denser, more intimately contacted morphology identified by SEM in Figure 2.

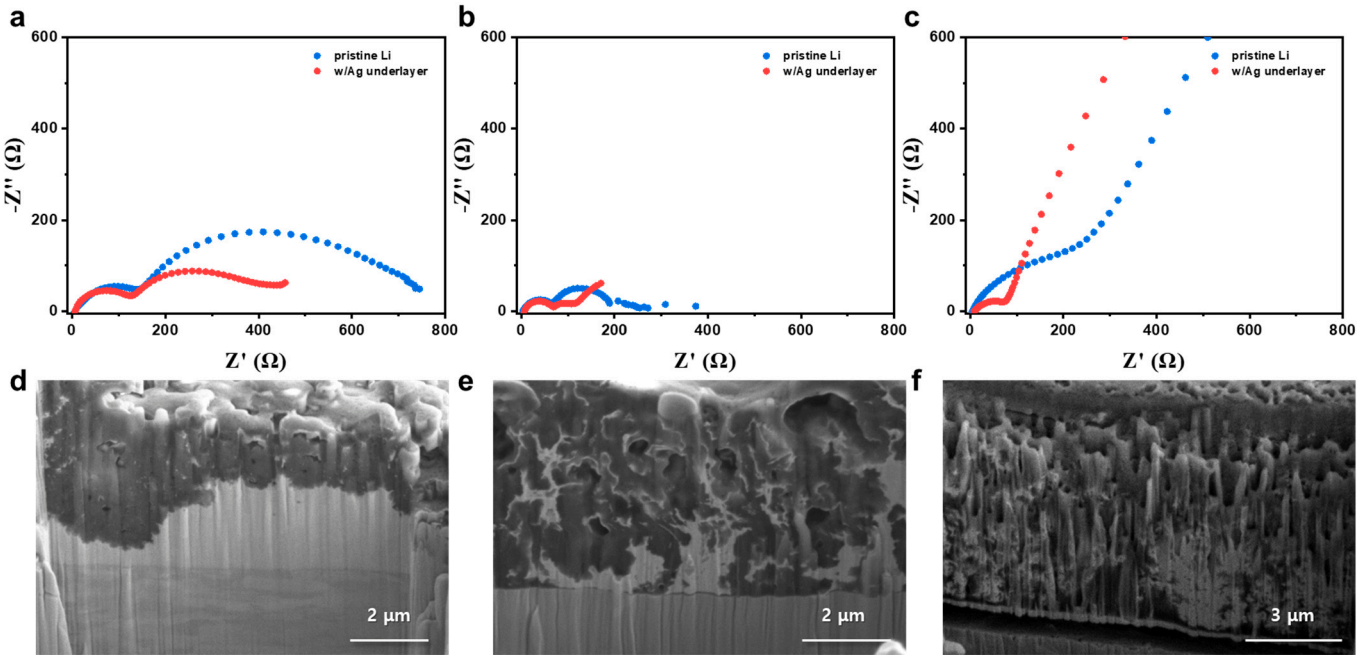


Figure 5. (**a**–**c**) Nyquist plots of symmetric Li//Li and Li–Ag//Li–Ag cells measured (**a**) before cycling, (**b**) after 10 cycles, and (**c**) after 50 cycles. (**d**–**f**) Cross-sectional FIB–SEM images of the Li–Ag//Li–Ag symmetric cell obtained (**d**) before cycling, (**e**) after 10 cycles, and (**f**) after 50 cycles.

After 10 cycles (Figure 5b), both electrodes show a marked collapse in impedance relative to their pre-cycling state, with the pristine Li and Li-Ag cells closing at approximately 400 Ω and 200 Ω, respectively. This overall decrease is consistent with the activation behavior commonly observed in Li metal cells, in which initial plating/stripping roughens the electrode and increases the electrochemically active area; the Li-Ag cell nonetheless retains a roughly two-fold lower impedance than the pristine Li cell at this stage, mirroring the lower overpotential observed in the galvanostatic cycling data (Figure 4). By 50 cycles (Figure 5c), the response of both cells no longer closes into a well-defined semicircle and instead rises steeply, reaching $-Z''$ values of approximately 700 Ω; the pristine Li cell reaches this magnitude at a real-axis value of approximately 570 Ω, while the Li-Ag cell reaches a comparable magnitude at a lower real-axis value of approximately 390 Ω. This steep, non-closing response is indicative of a growing resistive interphase, most likely associated with continued electrolyte decomposition and the accumulation of electrochemically inactive ("dead") Li, and its comparatively larger real-axis component for the pristine Li cell suggests that this degradation proceeds more extensively at the untreated Li interface.

To separate the overlapping contributions, the EIS spectra of the same cells measured before cycling and after 1, 10, and 50 cycles were analyzed by DRT and equivalent circuit fitting, as shown in Figures S6 and S7 and Table S1 [25]. The DRT spectra resolve an SEI process below 1 ms, a charge-transfer process between 1 ms and 1 s, and a low-frequency diffusion and blocking response. The SEI resistance of the pristine Li electrode increases continuously from 17.7 Ω after the first cycle to 67.6 and 216 Ω after 10 and 50 cycles, whereas that of the Li-Ag electrode remains below 75 Ω, indicating suppressed SEI accumulation.

Cross-sectional FIB-SEM images of the Li-Ag//Li-Ag cell (Figure 5d–f) corroborate this evolution. Before cycling (Figure 5d), the deposited film is dense and columnar, with a well-defined, low-porosity cross-section consistent with the morphology described in Figure 2. After 10 cycles (Figure 5e), the cross-section develops pronounced internal porosity and a heterogeneous, patchy contrast, indicative of localized dissolution/redeposition and early-stage restructuring of the interphase; this increase in internal surface area is consistent

with the reduced apparent impedance observed over the same interval (Figure 5b). After 50 cycles (Figure 5f), the film has evolved into a highly textured, columnar morphology spanning the full cross-section, reflecting substantial structural reorganization of the Li-Ag layer with continued cycling. Although rougher than the as-deposited state, it remains a continuous, adherent layer without the loosely packed, filamentary dendrites typically associated with catastrophic short-circuiting, consistent with the absence of failure observed for the Li-Ag electrode throughout extended galvanostatic cycling (Figure 4a).

3.6. Full-Cell Performance with NCM811 Cathode

To evaluate the practical relevance of the Li–Ag alloy anode, full cells were assembled by pairing the electrodes with a $LiNi_{0.8}Co_{0.1}Mn_{0.1}O_2$ (NCM811) cathode (areal capacity 1.0 mAh cm^{-2}) and cycled at 0.5 C between 2.9 and 4.2 V (Figure 6). The charge/discharge voltage profiles recorded at representative cycles (1, 3, 5, 10, and 30) are shown for the 5 µm pristine Li (Figure 6a) and 5 µm Li–Ag (Figure 6b) full cells. Both electrodes exhibit the sloping charge/discharge profiles characteristic of NCM811, but the polarization gap between the charge and discharge plateaus broadens markedly with cycling for the Li only cell, while it remains narrower and more stable for the Li–Ag electrode, reflecting the lower interfacial impedance associated with the Li–Ag alloy layer.

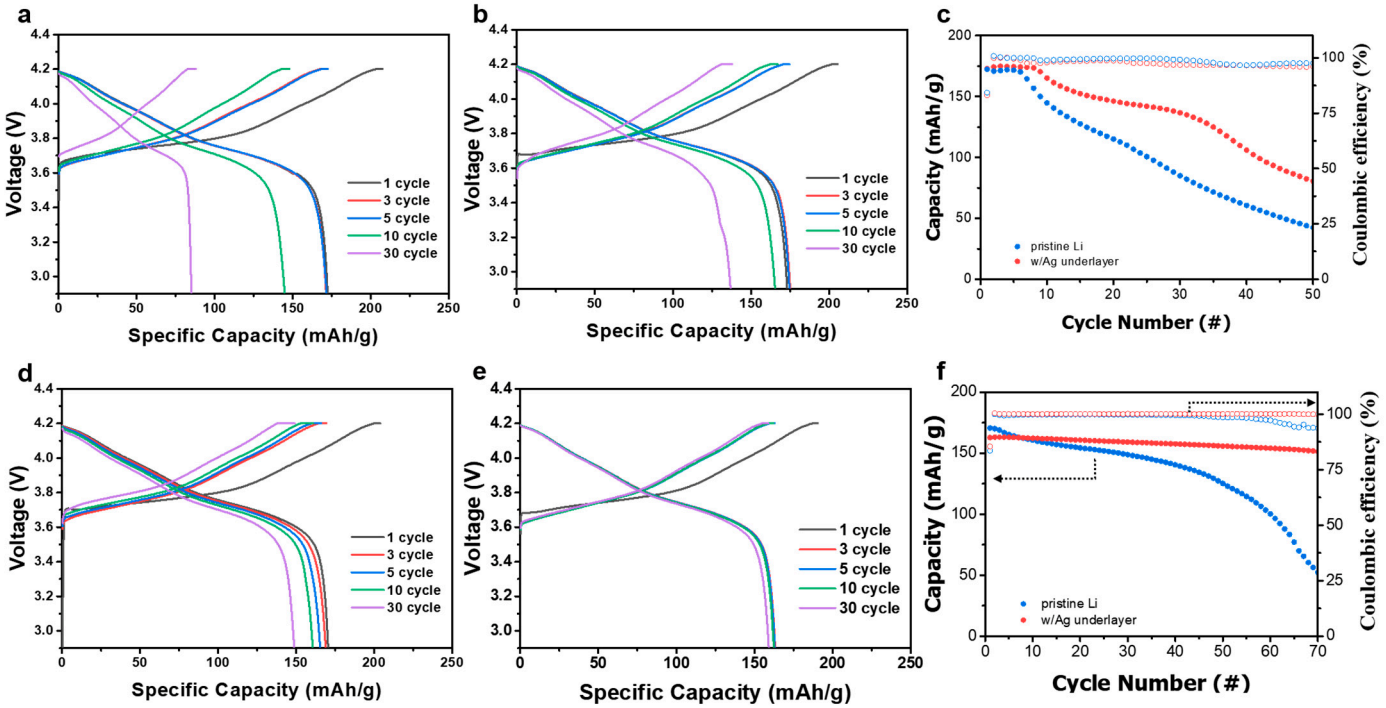


Figure 6. Full cell performance of Li//NCM811 and Li-Ag//NCM811 cells with Li thicknesses of 5 and 10 µm. (**a**,**b**) Charge–discharge voltage curves of 5 µm pristine Li electrode and 5 µm Li-Ag electrode (1st 3rd, 5th, 10th, and 30th cycles). (**c**) Specific discharge capacity and Coulombic efficiency of the 5 µm full cells during cycling. (**d**,**e**) Charge–discharge voltage curves of 10 µm pristine Li electrode and 10 µm Li-Ag electrode (1st 3rd, 5th, 10th, and 30th cycles). (**f**) Specific discharge capacity and Coulombic efficiency of the 10 µm full cells during cycling. All cells cycled at 0.5C between 2.9 and 4.2 V (hollow circle: Coulombic efficiency).

The specific-capacity retention and Coulombic efficiency as a function of cycle number is summarized in Figure 6c. Both cells deliver an initial discharge capacity of ~170 mAh g^{-1}, in line with the theoretical capacity of NCM811. After 50 cycles, the Li-Ag cell retains 80 mAh g^{-1}, whereas the Li–only cell ends at 45 mAh g^{-1} under the same protocol. The Coulombic efficiency recovers from an initial formation value of ~83% to a stable plateau of

95–98% for both cells, with the two curves nearly overlapping throughout the 50-cycle test. This indicates that the per-cycle reversibility is comparable for the two electrodes. Therefore, the improved capacity retention of the Li-Ag cell cannot be attributed to a reduction in parasitic reactions, but rather to the more stable Li/electrolyte interface and the suppression of local current concentration, as reflected in the narrower voltage hysteresis.

A similar trend is observed in the 10 μm pristine Li (Figure 6d) and 10 μm Li–Ag (Figure 6e) full cells. Increasing the Li thickness provides additional active Li, leading to improved cycling stability for both cells. Nevertheless, the Li-Ag cell exhibits more stable charge–discharge voltage profiles than the pristine Li cell throughout cycling. Up to the 30th cycle, the Li-Ag full cell exhibits negligible capacity fading, whereas the pristine Li cell retains only approximately 88% of its initial capacity.

After 70 cycles, the Li-Ag full cell maintains 160 mAh g^{-1}, whereas the Li–only cell ends at ~50 mAh g−1 under the same protocol (Figure 6f). Furthermore, the Coulombic efficiency of the Li-Ag cell remains stable throughout cycling, whereas that of the pristine Li cell begins to decrease noticeably after 60 cycles. These electrochemical results are in good agreement with the XPS and FIB-SEM observations discussed above, further supporting the beneficial role of the Ag layer in improving interfacial stability.

The comparatively modest absolute capacity retention of the Li–Ag full cell (~80 mAh g^{-1} after 50 cycles, ~47% of its initial value) is most plausibly related to the Ag underlayer thickness (~1 μm) used in this proof-of-concept, which consumes part of the initially deposited Li to form the alloy and thereby reduces the pool of electrochemically active Li available for reversible cycling against the capacity-limited NCM811 cathode. Based on the density and molar mass of Ag, a 1 μm Ag layer containing 9.72 μmol cm^{-2} of Ag would consume 0.26–0.59 mAh cm^{-2} of Li if fully converted to LiAg or Li_9Ag_4, i.e., 25–57% of the 5 μm Li film with a capacity of 1.03 mAh cm^{-2}, as summarized in Table S2. However, the delithiation tests in Figure S5 show a much smaller Li uptake. Even the 1 μm Ag electrode lithiated to 0.01 V with a potentiostatic hold delivered a reversible dealloying capacity of only 0.15 mAh cm^{-2}, corresponding to $x \approx 0.59$, which indicates a Li-poor Li-Ag alloy. The as-deposited Li-Ag electrode contains 0.08–0.14 mAh cm^{-2} of alloyed Li, corresponding to $x \approx 0.32$–0.54 and to only 8–14% of the initial Li inventory. Because this Li is extracted only at about 0.3 V vs. Li/Li^+, it contributes little to the usable capacity of the capacity-balanced full cell. This dead-Li penalty is masked in the Li-excess symmetric-cell configuration (Figure 4) but becomes more apparent in the capacity-balanced full cell. Optimizing the Ag/Li thickness ratio, for example by reducing the Ag thickness while retaining its interfacial benefits, represents a clear direction for further improving full-cell capacity retention.

The Ag layer also adds a mass of 1.05 mg cm^{-2} per μm, about four times that of a 5 μm Li film. Because the full cell energy is fixed by the cathode, the active material level specific energy decreases by about 15% for 1 μm Ag but only by about 1.7% for 0.1 μm Ag, as listed in Table S2. Since both the Li consumption and the mass penalty scale linearly with the Ag thickness, the Ag layer should be reduced to the minimum required for continuous lithiophilic coverage. Based on the measured Li uptake with $x \approx 0.59$, the fraction of Li lost is about 0.75 times the Ag/Li thickness ratio. An Ag/Li thickness ratio of 0.13 or less therefore keeps the Li loss below 10%, and a ratio of 0.067 or less, corresponding to 330 nm of Ag for 5 μm of Li, keeps it below 5%, although the minimum Ag thickness for continuous coverage remains to be determined experimentally.

4. Conclusions

We have demonstrated an in situ alloying strategy for stabilizing evaporated ultra-thin Li metal anodes by introducing a thin Ag interlayer that spontaneously alloys with the subsequently evaporated Li. The layer-by-layer stacked architecture of Li/Ag is produced

via dual-source thermal evaporation without any air-exposure. Through the cross-sectional SEM with EDS mapping and air-free XPS analysis, bottom Ag layer is redistributed into upper Li layer and alloyed thin film yields denser and finer-grained film with reduction in surface roughness. Furthermore, in situ alloyed thin film Li film exhibits electrochemical performance that substantially extends the cycle life of symmetric cells (more than doubling it at 0.5 mA cm^{-2} and demonstrating stable operation over 200 cycles at 0.1 mA cm^{-2}), while sustaining a markedly lower and more symmetric polarization. In NCM811 full cells, the Li-Ag anode delivers narrower voltage hysteresis compared to the pristine Li electrode, alongside enhanced capacity retention, with more stable Coulombic efficiency evident at the greater (10 μm) Li thickness. In situ vacuum alloying represents a scalable, impurity-free route for fabricating dendrite-resistant ultra-thin Li metal anodes, providing a practical and broadly applicable strategy for next-generation high-energy-density Li metal batteries.

Nevertheless, the 1 μm Ag layer used in this proof-of-concept consumes 8–14% of the Li inventory, adds mass, and corresponds to about 10.5 g of Ag per m^2 of electrode, or about 17 USD m^{-2} at a silver price of about 1.6 USD g^{-1}. Because these penalties scale linearly with the Ag thickness, reducing the Ag layer to the tens-of nanometers scale would lower them by more than an order of magnitude, and lower cost lithiophilic elements such as Zn, Mg, and Al offer an alternative. Combined with source-material recovery in vacuum deposition and the small electrode areas of on-chip micro-batteries, this provides a practical route toward industrial application.

Supplementary Materials: The following supporting information can be downloaded at https://www.mdpi.com/article/10.3390/batteries12110495/s1, Figure S1: Photographs of the Li and Li-Ag electrodes immediately after deposition and after 24 h of storage under Ar atmosphere; Figure S2: SEM images of the Ag-decorated Li electrode at low and high magnification; Figure S3: Air-free XPS transfer holder and XPS survey spectra of the pristine Li and Li-Ag electrodes; Figure S4: Air-free XPS depth profiles and Ag Auger parameter analysis; Figure S5: Delithiation profiles and dQ/dV curves of the Li, Li-Ag, and lithiated Ag electrodes; Figure S6: EIS and DRT analysis of the Li//Li and Li-Ag//Li-Ag symmetric cells before cycling and after 1, 10, and 50 cycles; Figure S7: Equivalent circuits and fits for the individual impedance spectra of the Li//Li and Li-Ag//Li-Ag symmetric cells before cycling and after 1, 10, and 50 cycles; Table S1: Interfacial resistances obtained from equivalent circuit fitting and DRT peak integration for the pristine Li and Li-Ag symmetric cells; Table S2: Li consumption by alloying, added mass, and relative specific energy as a function of Ag thickness.

Author Contributions: Conceptualization, H.K. and S.-H.C.; methodology, H.K., S.L. and S.-H.C.; investigation, H.K., S.L., Y.C., and S.H.; review and editing, C.W.A. and H.H.; supervision, S.-S.K., H.S. and S.-H.C. All authors have read and agreed to the published version of the manuscript.

Funding: This research was funded by the Nano & Material Technology Development Program through the National Research Foundation of Korea (NRF) funded by Ministry of Science and ICT (no. RS-2024-00450477).

Data Availability Statement: The data presented in this study are available on request from the corresponding authors.

Acknowledgments: This research was funded by the Nano & Material Technology Development Program through the National Research Foundation of Korea (NRF) funded by Ministry of Science and ICT (no. RS-2024-00450477). This work was also supported by Semiconductor-Secondary Battery Interfacing Platform Technology Development Project and Innovative Company Pilot Production Development Support Project of NNFC in 2026. During the preparation of this study, the authors used ChatGPT 5.4 for the purposes of language refinement. The authors have reviewed and edited the output and take full responsibility for the content of this publication.

Conflicts of Interest: The authors declare no conflicts of interest.

References

1. Khan, F.N.U.; Rasul, M.G.; Sayem, A.; Mandal, N. Maximizing energy density of lithium-ion batteries for electric vehicles: A critical review. *Energy Rep.* **2023**, *9*, 11–21. [CrossRef]
2. Ngoy, K.R.; Lukong, V.T.; Yoro, K.O.; Makambo, J.B.; Chukwuati, N.C.; Ibegbulam, C.; Eterigho-Ikelegbe, O.; Ukoba, K.; Jen, T.-C. Lithium-ion batteries and the future of sustainable energy: A comprehensive review. *Renew. Sustain. Energy Rev.* **2025**, *223*, 115971. [CrossRef]
3. Asenbauer, J.; Eisenmann, T.; Kuenzel, M.; Kazzazi, A.; Chen, Z.; Bresser, D. The success story of graphite as a lithium-ion anode material–fundamentals, remaining challenges, and recent developments including silicon (oxide) composites. *Sustain. Energy Fuels* **2020**, *4*, 5387–5416. [CrossRef]
4. Zhang, H.; Yang, Y.; Ren, D.; Wang, L.; He, X. Graphite as anode materials: Fundamental mechanism, recent progress and advances. *Energy Storage Mater.* **2021**, *36*, 147–170. [CrossRef]
5. Nzereogu, P.; Omah, A.; Ezema, F.; Iwuoha, E.; Nwanya, A. Anode materials for lithium-ion batteries: A review. *Appl. Surf. Sci. Adv.* **2022**, *9*, 100233. [CrossRef]
6. Xu, W.; Wang, J.; Ding, F.; Chen, X.; Nasybulin, E.; Zhang, Y.; Zhang, J.-G. Lithium metal anodes for rechargeable batteries. *Energy Environ. Sci.* **2014**, *7*, 513–537. [CrossRef]
7. Liu, B.; Zhang, J.-G.; Xu, W. Advancing lithium metal batteries. *Joule* **2018**, *2*, 833–845. [CrossRef]
8. Ko, S.; Obukata, T.; Shimada, T.; Takenaka, N.; Nakayama, M.; Yamada, A.; Yamada, Y. Electrode potential influences the reversibility of lithium-metal anodes. *Nat. Energy* **2022**, *7*, 1217–1224. [CrossRef]
9. Li, L.; Li, S.; Lu, Y. Suppression of dendritic lithium growth in lithium metal-based batteries. *Chem. Commun.* **2018**, *54*, 6648–6661. [CrossRef] [PubMed]
10. Kang, S.; Cheng, J.; Gao, W.; Cui, L. Toward safer lithium metal batteries: A review. *Energy Mater.* **2023**, *3*, 300043. [CrossRef]
11. Yan, K.; Lu, Z.; Lee, H.-W.; Xiong, F.; Hsu, P.-C.; Li, Y.; Zhao, J.; Chu, S.; Cui, Y. Selective deposition and stable encapsulation of lithium through heterogeneous seeded growth. *Nat. Energy* **2016**, *1*, 16010. [CrossRef]
12. Cheng, X.-B.; Zhang, R.; Zhao, C.-Z.; Zhang, Q. Toward safe lithium metal anode in rechargeable batteries: A review. *Chem. Rev.* **2017**, *117*, 10403–10473. [CrossRef] [PubMed]
13. Zhang, R.; Chen, X.R.; Chen, X.; Cheng, X.B.; Zhang, X.Q.; Yan, C.; Zhang, Q. Lithiophilic sites in doped graphene guide uniform lithium nucleation for dendrite-free lithium metal anodes. *Angew. Chem.* **2017**, *129*, 7872–7876. [CrossRef]
14. Albertus, P.; Babinec, S.; Litzelman, S.; Newman, A. Status and challenges in enabling the lithium metal electrode for high-energy and low-cost rechargeable batteries. *Nat. Energy* **2018**, *3*, 16–21. [CrossRef]
15. Lee, J.; Jeong, S.H.; Nam, J.S.; Sagong, M.; Ahn, J.; Lim, H.; Kim, I.D. Toward thin and stable anodes for practical lithium metal batteries: A review, strategies, and perspectives. *EcoMat* **2023**, *5*, e12416. [CrossRef]
16. Fang, C.; Wang, X.; Meng, Y.S. Key issues hindering a practical lithium-metal anode. *Trends Chem.* **2019**, *1*, 152–158. [CrossRef]
17. Ho, A.S.; Westover, A.S.; Browning, K.; Maslyn, J.A.; Parkinson, D.Y.; Sahore, R.; Dudney, N.; Balsara, N.P. Comparing the purity of rolled versus evaporated lithium metal films using X-ray microtomography. *ACS Energy Lett.* **2022**, *7*, 1120–1124. [CrossRef]
18. Hou, Z.; Yu, Y.; Wang, W.; Zhao, X.; Di, Q.; Chen, Q.; Chen, W.; Liu, Y.; Quan, Z. Lithiophilic Ag nanoparticle layer on Cu current collector toward stable Li metal anode. *ACS Appl. Mater. Interfaces* **2019**, *11*, 8148–8154. [CrossRef] [PubMed]
19. Park, Y.-E.; Oh, M.-K.; Sim, H.-T.; Kim, H.-J.; Cho, Y.-S.; Park, S.-J.; Kim, D.-W. Rationally Designed Li–Ag Alloy with In-Situ-Formed Solid Electrolyte Interphase for All-Solid-State Lithium Batteries. *ACS Appl. Mater. Interfaces* **2024**, *16*, 39460–39469. [CrossRef] [PubMed]
20. Zhao, Y.; Li, S.; Huang, X.; Chen, W.; Wang, C.; Tang, X.; Dou, H.; Zhang, X. Vacuum evaporation plating enabling ≤10 μm ultrathin lithium foils for lithium metal batteries. *Small* **2024**, *20*, 2312129. [CrossRef] [PubMed]
21. Hu, Y.; Chen, Z.; Wang, Y.; Hou, H.; Chen, B.; Mitlin, D.; Liu, W. Review of thin lithium metal battery anode fabrication–microstructure–electrochemistry relations. *Adv. Mater.* **2026**, *38*, e11817. [CrossRef] [PubMed]
22. Acebedo, B.; Cid, R.; de Lasen-Tejada, M.; Morant-Minana, M.C.; Fallarino, L.; Goikolea, E.; Rikarte, J.; Gonzalo, E.; de Larramendi, I.R. On the role of ultrathin lithium metal anodes produced by thermal evaporation. *J. Power Sources* **2024**, *618*, 235218. [CrossRef]
23. Pelton, A.D. The Ag-Li (Silver-Lithium) System. *Bull. Alloy Phase Diagr.* **1986**, *7*, 223–228. [CrossRef]
24. Machocki, A.; Ioannides, T.; Stasinska, B.; Gac, W.; Avgouropoulos, G.; Delimaris, D.; Grzegorczyk, W.; Pasieczna, S. Manganses-lanthanum oxides modified with silver for the catalytic combusition of methane. *J. Catal.* **2004**, *227*, 282–296. [CrossRef]
25. Wan, T.H.; Sccoccio, M.; Chen, C.; Ciucci, F. Influence of the Discretization Methods on the Distribution of Relaxation Times Deconvolution: Implementing Radial Basis Functions with DRTtools. *Electrochim. Acta* **2015**, *184*, 483–499. [CrossRef]

Disclaimer/Publisher's Note: The statements, opinions and data contained in all publications are solely those of the individual author(s) and contributor(s) and not of MDPI and/or the editor(s). MDPI and/or the editor(s) disclaim responsibility for any injury to people or property resulting from any ideas, methods, instructions or products referred to in the content.